Article

DC Admittance Model of VSCs for Stability Studies in VSC-HVDC Systems

Joaquín Pedra [1,*], Luis Sainz [1] and Lluís Monjo [2]

1   Department of Electrical Engineering (ETSEIB—UPC), Universitat Politècnica de Catalunya, Av. Diagonal 647, 08028 Barcelona, Spain; luis.sainz@upc.edu
2   Department of Electrical Engineering (EPSEVG—UPC), Universitat Politècnica de Catalunya, Av. Victor Balaguer s/n, 08800 Vilanova i La Geltrú, Spain; lluis.monjo@upc.edu
*   Correspondence: joaquin.pedra@upc.edu

Abstract: High-voltage direct current (HVDC) systems linked to AC grids with converters are promising energy transmission systems. These systems present complex AC- and DC-side dynamic interactions. Impedance-based stability studies have recently been proposed to assess DC-side dynamics from DC-side characterization of voltage source converters (VSCs) considering AC-side dynamics. However, the existing approaches used for stability studies in VSC-HVDC systems do not completely model VSCs because they do not consider together the VSC delay, the grid voltage feedforward filter, and all the d- and q-reference current controls. Moreover, these approaches are analytically characterized from dq-real space vectors (less related to circuit theory than dq-complex space vectors), and some work with simple AC grids. The main contribution of this paper is a detailed and complete DC admittance model of VSCs from dq-complex space vectors, which considers the VSC delay, feedforward filter, and d- and q-reference current controls, and also a general AC grid. The proposed model can be used for DC-side stability studies in VSC-HVDC systems considering AC grid dynamics. The capabilities and drawbacks of impedance-based stability methods for DC-side stability assessment were analyzed, and the positive-net-damping criterion was validated as a robust approach. The model was validated by PSCAD/EMTDC simulations and applied to a stability study in a VSC-HVDC system.

Keywords: impedance modeling; voltage source converters; HVDC transmission

1. Introduction

VSC-HVDC systems are emerging as a future transmission energy technology [1]. Near-synchronous [1–3] and harmonic [4,5] oscillatory instabilities due to low-damped resonances are a usual concern in these systems, and their accurate assessment is challenging for researchers. The state-space and frequency-domain methods are the most common approaches used to analyze these oscillatory phenomena [1–10]. The state-space method [3] is a global stability approach (i.e., stability is determined regardless of location [2]) but uses high-order dynamic models and requires specific information about all system elements, which is not always accessible. On the other hand, the frequency-domain methods assess system stability with less computing effort than the state-space method and are used either with simulations or system measurements. Broadly speaking, frequency-domain methods are applied using impedance-based stability criteria, such as the Nyquist criterion [4–6], impedance-based analysis [1], and the positive-net-damping stability criterion [4–9] for load–source equivalent systems, and the generalized Nyquist criterion (GNC) [2,6,10] and impedance matrix determinant analysis [3] for interconnected systems. Most of these criteria are local stability approaches (i.e., they are locally applied) sensitive to system partitions, which can lead to inaccurate stability predictions.

This weakness has been discussed in the literature to understand the proper application of the different criteria [2].

Stability studies in HVDC systems require DC-side equivalent modeling of converters. Early studies on VSC-HVDC systems considered weak and simple *R–L* AC grids and a few VSC controls to obtain the DC-side model of VSCs [4,9]. This, in general, leads to inaccurate stability predictions because AC-side and VSC control dynamics are overlooked. Improved DC-side models of VSCs that consider AC-side dynamics have recently been proposed [11–15]. The first DC-side equivalent model for VSC rectifier and inverter stations of VSC-HVDC systems with active power and DC voltage controls, respectively, and grid alternating voltage control is derived from *dq*-real space vectors in [11]. The model disregards the VSC delay and phase-locked loop (PLL) control. Moreover, the study considers a simple *R–L* impedance on the AC-side and wrongly concludes that AC-side instabilities are not detected on the DC side. A DC-side equivalent admittance model of a VSC-HVDC station in an offshore wind farm with DC voltage and PLL controls using *dq*-real space vectors is presented in [12]. Additionally, the modified sequence and phasor-domain models are derived from the previous model. The model disregards the VSC delay, grid voltage feedforward filter, and *q*-reference current controls. A general AC grid characterization to correctly analyze the influence of AC-side dynamics on DC-side instabilities (e.g., the mirror frequency effect [6,16]) is also considered in [12]. A DC impedance model of VSC rectifier and inverter stations of VSC-HVDC systems with active power and DC voltage controls, respectively, and PLL control is derived by using *dq*-real space vectors in [13–15]. The VSC delay and a general AC grid are also considered, but the grid voltage feedforward filter and the *q*-reference current controls are disregarded.

The above comments are summarized in Table 1. The first row (labeled "Phase-locked loop control") shows the models in which the PLL control is included. The second row (labeled "VSC delay") shows the models in which the VSC time delay transfer function is included. The third and fourth rows show the models which use voltage feedforward without and with a low-pass filter. The fifth and sixth rows show the models which include the outer control loops on channels *d* and *q*.

Table 1. Comparison of models.

Model Feature	References					Proposed Model
	[11]	[12]	[13]	[14]	[15]	
Phase-locked loop control	✘	✔	✔	✔	✘	✔
VSC delay	✘	✘	✔	✔	✘	✔
Grid voltage feedforward	✘	✘	✔	✔	✔	✔
Grid voltage feedforward filter	✘	✘	✘	✘	✘	✔
D-outer control loop	✔	✔	✔	✔	✔	✔
Q-outer control loop	✘	✘	✘	✘	✔	✔

The influence of AC-side dynamics on stability and the stability assessment using the impedance-based stability criteria have been discussed. To better explain frequency coupling dynamics between the AC and DC sides (i.e., the mirror frequency effect), modified sequence [16] and *dq*-complex-domain [17] approaches have been proposed from the *dq*-real-domain model based on the Park (*dq*-real) and Ku (*dq*-complex) transformations [18]. Both *dq*-real- and *dq*-complex-domain approaches can be used for VSC modeling, but they have advantages and disadvantages for Laplace and frequency studies of grid-connected VSC stability:

- *dq*-real-domain approach:
    - Laplace stability studies: It allows system poles and participation factors to be easily obtained but is not appropriate for integrating components of large power

systems. Moreover, frequency black-box models obtained from measurements cannot be used with this approach.

- – Frequency stability studies: It is the most used in the literature [11–15] but reducing AC networks to their equivalent Thevenin circuit in *dq*-real variables is more laborious than in *dq*-complex variables. This is because AC-side impedances are 2 × 2 matrices with *dq*-real variables.

- *dq*-complex-domain approach:
  - – Laplace stability studies: The characterization of system poles poses numerical problems because of rounding errors produced by the complex coefficients of *dq*-complex-domain transfer functions. Polynomials in the *s*-domain with only real coefficients are required in the DC impedance to correctly obtain the system poles.
  - – Frequency stability studies: It has recently been used in the literature [19,20]. In the *dq*-complex domain, the AC-side elements use the impedances $Z_{Th}(s + j\omega_1)$ and $Z_{Th}(s - j\omega_1)$ obtained by shifting the operational Thevenin impedance $Z_{Th}(s)$. The *dq*-complex domain is more appropriate for integrating VSC models in large power systems.

According to the above comments, the benefits of the *dq*-complex-domain approach over the *dq*-real-domain approach for grid impedance modeling and stability studies are greater.

This paper contributes to filling the above gaps in the characterization of the DC admittance model of VSCs. Moreover, it studies the inaccuracies of impedance-based stability criteria due to partitions in VSC-HVDC systems in two ways. The first contribution is a novel DC admittance model for VSCs based on *dq*-complex space vectors. The model extends existing models by considering the VSC delay, grid voltage feedforward filter, PLL, and main *d*-reference (active power and DC voltage controls) and *q*-reference (reactive power and grid alternating voltage controls) current outer loops, and also a general AC grid. The second contribution involves the study of VSC-HVDC system stability. The sensitivity of impedance-based stability criteria to VSC-HVDC system partitions is discussed, and the positive-net-damping stability criterion is proposed to overcome this issue. Finally, the influence of AC-side dynamics on the DC-side stability of VSC-HVDC systems was analyzed. The stability issues in a VSC-HVDC system were studied with the proposed DC admittance model to show the paper's contribution. PSCAD/EMTDC simulations were performed to validate the study.

2. Model of VSCs in DQ-Complex Domain

Complex transfer functions are used in this section to model VSCs with *dq*-complex space vectors [6,16,17]. This approach is used in the next section to obtain the DC admittance of the VSCs.

The Laplace variable *s* will be omitted in the *dq*-complex transfer functions hereinafter to simplify notation, and the *dq*-complex space vectors are defined as $\mathbf{U_{dq}} = (U_d + jU_q)/\sqrt{2}$ and $\mathbf{I_{dq}} = (I_d + jI_q)/\sqrt{2}$.

2.1. AC Grid Relations

The relation between voltage and current at the point of common coupling in Figure 1 is expressed as

$$\begin{bmatrix} \Delta \mathbf{E_{dq}} \\ \Delta \mathbf{E_{dq}^*} \end{bmatrix} = - \begin{bmatrix} \mathbf{Z_{Th}^+} & \mathbf{Z_{Th}^-} \\ (\mathbf{Z_{Th}^-})^* & (\mathbf{Z_{Th}^+})^* \end{bmatrix} \begin{bmatrix} \Delta \mathbf{I_{dq}} \\ \Delta \mathbf{I_{dq}^*} \end{bmatrix} \quad \Rightarrow \quad \Delta \mathbf{E_{dq}^m} = -\mathbf{Z_{Th}^\pm} \Delta \mathbf{I_{dq}^m}, \tag{1}$$

where $\mathbf{Z_{Th}^+} = Z_{Th}(s + j\omega_1)$, $(\mathbf{Z_{Th}^+})^* = Z_{Th}(s - j\omega_1)$ and $\mathbf{Z_{Th}^-} = 0$. The voltage balance across the converter $R_c - L_c$ filter [20] is expressed as

$$\begin{bmatrix} \Delta\mathbf{V_{dq}} \\ \Delta\mathbf{V_{dq}^*} \end{bmatrix} = -\begin{bmatrix} \mathbf{Z_c^+} & \mathbf{Z_c^-} \\ (\mathbf{Z_c^-})^* & (\mathbf{Z_c^+})^* \end{bmatrix} \begin{bmatrix} \Delta\mathbf{I_{dq}} \\ \Delta\mathbf{I_{dq}^*} \end{bmatrix} + \begin{bmatrix} \Delta\mathbf{E_{dq}} \\ \Delta\mathbf{E_{dq}^*} \end{bmatrix} \quad \Rightarrow \quad \Delta\mathbf{V_{dq}^m} = -\mathbf{Z_c^{\pm}}\Delta\mathbf{I_{dq}^m} + \Delta\mathbf{E_{dq'}^m} \quad (2)$$

where $\mathbf{Z_c^+} = R_c + L_c(s + j\omega_1)$, $(\mathbf{Z_c^+})^* = R_c + L_c(s - j\omega_1)$, and $\mathbf{Z_c^-} = 0$.
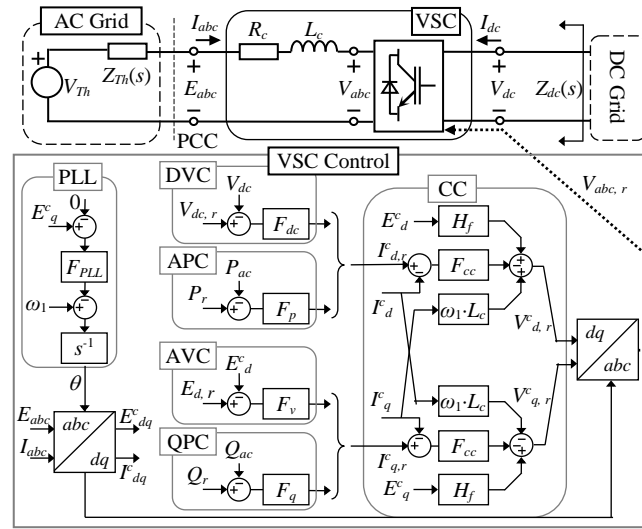

Figure 1. Grid-connected VSC system for DC impedance characterization.

Note that $\mathbf{Z_{Th}^-} = \mathbf{Z_c^-} = 0$ because the grid and the $R_c - L_c$ filter are three-phase symmetric systems whose impedance matrices in the dq-domain verify the relations $Z_{dd}(s) = Z_{qq}(s)$ and $Z_{dq}(s) = -Z_{qd}(s)$. Considering the above, the terms $\mathbf{Z_{Th}^+}$ and $\mathbf{Z_c^+}$ can also be expressed by using the coordinate transformation properties $\mathbf{Z_{Th}^+} = Z_{Th}(s + j\omega_1)$ and $\mathbf{Z_c^+} = Z_c(s + j\omega_1)$ $= R_c + L_c(s + j\omega_1)$ [6].

The relation between VSC output voltage and AC current is derived from (1) and (2):

$$\Delta\mathbf{V_{dq}^m} = -\mathbf{Z_t^{\pm}}\Delta\mathbf{I_{dq}^m} \quad \mathbf{Z_t^{\pm}} = (\mathbf{Z_c^{\pm}} + \mathbf{Z_{Th}^{\pm}}), \quad (3)$$

where $\mathbf{Z_t^+} = Z_t(s + j\omega_1)$ and $Z_t(s) = Z_{Th}(s) + R_c + L_c s$ is the AC impedance.

2.2. DC-AC Converter Relations

The relation between the VSC output voltage and the DC voltage and the relation between the DC and AC currents are expressed [20] as

$$\begin{bmatrix} \Delta\mathbf{V_{dq}} \\ \Delta\mathbf{V_{dq}^*} \end{bmatrix} = \begin{bmatrix} \Delta\mathbf{m_{dq}} \\ \Delta\mathbf{m_{dq}^*} \end{bmatrix} V_{dc0} + \begin{bmatrix} \mathbf{m_{dq0}} \\ \mathbf{m_{dq0}^*} \end{bmatrix} \Delta V_{dc} \Rightarrow \Delta\mathbf{V_{dq}^m} = \Delta\mathbf{m_{dq}^m} V_{dc0} + \mathbf{m_{dq0}^m}\Delta V_{dc}, \quad (4)$$

$$\Delta I_{dc} = -\begin{bmatrix} \mathbf{m_{dq0}^*} & \mathbf{m_{dq0}} \end{bmatrix} \begin{bmatrix} \Delta\mathbf{I_{dq}} \\ \Delta\mathbf{I_{dq}^*} \end{bmatrix} - \begin{bmatrix} \mathbf{I_{dq0}^*} & \mathbf{I_{dq0}} \end{bmatrix} \begin{bmatrix} \Delta\mathbf{m_{dq}} \\ \Delta\mathbf{m_{dq}^*} \end{bmatrix}$$
$$\Rightarrow \Delta I_{dc} = -(\mathbf{m_{dq0}^m})^H \Delta\mathbf{I_{dq}^m} - (\mathbf{I_{dq0}^m})^H \Delta\mathbf{m_{dq'}^m} \quad (5)$$

where $\mathbf{m_{dq}} = (m_d + jm_q)/\sqrt{2}$ and $\mathbf{I_{dq0}} = (I_{d0} + jI_{q0})/\sqrt{2}$, and the superscript H indicates the transpose and complex conjugate (Hermitian conjugate). Note that the three-phase set of modulation functions $\{m_a, m_b, m_c\} = M\{\cos(\omega_1 t + \phi_m), \cos(\omega_1 t + \phi_m - 2\pi/3), \cos(\omega_1 t + \phi_m + 2\pi/3)\}$ is transformed into the dq-complex space vector $\mathbf{m_{dq}} = (\sqrt{3}/2)M\angle\phi_m$ by applying the normalized Ku (dq-complex) transformation [6,18].

2.3. Simplified Model #1: Case without Current Control

In the case without current control, the modulation function is constant, $\Delta \mathbf{m}^*_{\mathbf{dq}} = 0$. Then, (4) and (5) result in

$$\Delta \mathbf{V}^{\mathbf{m}}_{\mathbf{dq}} = \mathbf{m}^{\mathbf{m}}_{\mathbf{dq0}} \Delta V_{dc} \ \ \Delta I_{dc} = -(\mathbf{m}^{\mathbf{m}}_{\mathbf{dq0}})^H \Delta \mathbf{I}^{\mathbf{m}}_{\mathbf{dq}}. \tag{6}$$

By considering (3) and (6), the DC admittance is

$$\Delta I_{dc} = Y_{dc} \Delta V_{dc} \ \ Y_{dc} = (\mathbf{m}^{\mathbf{m}}_{\mathbf{dq0}})^H (\mathbf{Z}^{\pm}_{\mathbf{t}})^{-1} \mathbf{m}^{\mathbf{m}}_{\mathbf{dq0}}, \tag{7}$$

where

$$
\begin{aligned}
Y_{dc} &= \begin{bmatrix} \mathbf{m}^*_{\mathbf{dq0}} & \mathbf{m}_{\mathbf{dq0}} \end{bmatrix} \begin{bmatrix} \mathbf{Z}^+_{\mathbf{t}} & 0 \\ 0 & (\mathbf{Z}^+_{\mathbf{t}})^* \end{bmatrix}^{-1} \begin{bmatrix} \mathbf{m}_{\mathbf{dq0}} \\ \mathbf{m}^*_{\mathbf{dq0}} \end{bmatrix} = \frac{3M^2}{4} \left(\frac{1}{\mathbf{Z}^+_{\mathbf{t}}} + \frac{1}{(\mathbf{Z}^+_{\mathbf{t}})^*} \right) \\
\mathbf{Z}^+_{\mathbf{t}} &= Z_t(s + j\omega_1) = Z_{Th}(s + j\omega_1) + R_c + L_c(s + j\omega_1) \\
(\mathbf{Z}^+_{\mathbf{t}})^* &= Z^*_t(s + j\omega_1) = Z_{Th}(s - j\omega_1) + R_c + L_c(s - j\omega_1),
\end{aligned}
\tag{8}
$$

and the DC impedance is the inverse of the DC admittance, $Z_{dc} = 1/Y_{dc}$.

The AC grid is represented by the circuit in Figure 2 [12], with the Thevenin transfer function written as

$$Z_{Th}(s) = \frac{1}{\frac{1}{R_g + L_g s} + \frac{1}{Z_f(s)}} \ ; \ Z_f(s) = \frac{1}{C_f s} + \frac{1}{\frac{1}{L_f s} + \frac{1}{R_f}}. \tag{9}$$
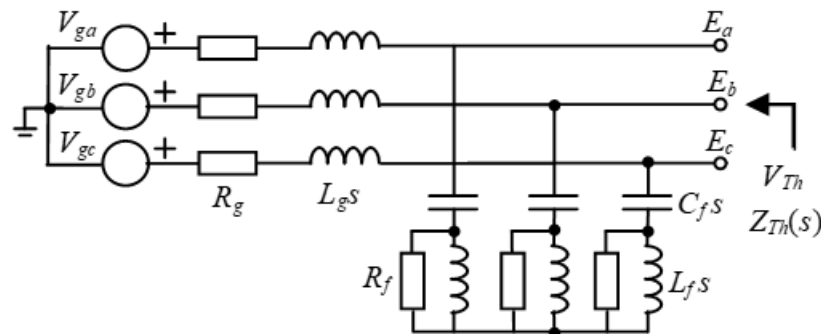
Figure 2. AC grid connected at the VSC terminals [12].

Note that the frequency response of a conjugate transfer function such as $(\mathbf{Z}^+_{\mathbf{t}})^*(s)$ in (8) can be calculated as [19].

$$Z^*(s) = [Z(s^*)]^* \ \Rightarrow \ Z^*(j\omega) = [Z(-j\omega)]^*. \tag{10}$$

2.4. Simplified Model #2: Case with Current Control

Only the modulation function and current control of the VSC with delay are considered. Then, the current control loop [20] is expressed as

$$\Delta \mathbf{V}^{\mathbf{m}}_{\mathbf{dq, r}} = \mathbf{F}^{\pm}_{\mathbf{cc}} \Delta \mathbf{I}^{\mathbf{m}}_{\mathbf{dq}} - \mathbf{Z}^{\pm}_{\boldsymbol{\omega}} \Delta \mathbf{I}^{\mathbf{m}}_{\mathbf{dq}} + \mathbf{H}^{\pm}_{\mathbf{f}} \Delta \mathbf{E}^{\mathbf{m}}_{\mathbf{dq}}, \tag{11}$$

where $\mathbf{F}^+_{\mathbf{cc}} = D(s)F_{cc}(s)$, $\mathbf{Z}^+_{\boldsymbol{\omega}} = D(s) \cdot jL_c\omega_1$, $\mathbf{H}^+_{\mathbf{f}} = D(s)H_f(s)$, and $\mathbf{F}^-_{\mathbf{cc}} = \mathbf{Z}^-_{\boldsymbol{\omega}} = \mathbf{H}^-_{\mathbf{f}} = 0$, with $D(s) = e^{-sT_d}$ being the VSC time delay transfer function, $F_{scc}(s) = k_{sp, cc} + k_{si, cc}/s$, and $H_f(s) = \alpha_f/(s + \alpha_f)$, with $k_{sp, cc}$ and $k_{si, cc}$ being the proportional and integral gains of the current control, α_f being the bandwidth of the voltage feedforward low-pass filter, and T_d being the VSC time delay. The VSC reference voltage, $\Delta \mathbf{V}^{\mathbf{m}}_{\mathbf{dq, r}} = V_{dc0} \Delta \mathbf{m}^{\mathbf{m}}_{\mathbf{dq}}$ (11), is the *dq*-complex space vector determining the modulation function:

$$\Delta \mathbf{m_{dq}^m} = \frac{1}{V_{dc0}} \left(\mathbf{Z_{pi}^{\pm}} \Delta \mathbf{I_{dq}^m} + \mathbf{H_f^{\pm}} \Delta \mathbf{E_{dq}^m} \right) ; \ \mathbf{Z_{pi}^{\pm}} = \mathbf{F_{cc}^{\pm}} - \mathbf{Z_{\omega}^{\pm}}. \tag{12}$$

By considering (1) and (12), (5) becomes

$$\Delta I_{dc} = \left[-(\mathbf{m_{dq0}^m})^H - \frac{(\mathbf{I_{dq0}^m})^H}{V_{dc0}} \left(\mathbf{Z_{pi}^{\pm}} - \mathbf{H_f^{\pm}} \mathbf{Z_{Th}^{\pm}} \right) \right] \Delta \mathbf{I_{dq}^m}, \tag{13}$$

and (4) can be expressed from (1), (2), and (12) as

$$\Delta \mathbf{V_{dq}^m} = -\mathbf{Z_c^{\pm}} \Delta \mathbf{I_{dq}^m} + \Delta \mathbf{E_{dq}^m} = -(\mathbf{Z_c^{\pm}} + \mathbf{Z_{Th}^{\pm}}) \Delta \mathbf{I_{dq}^m} = \left(\mathbf{Z_{pi}^{\pm}} - \mathbf{H_f^{\pm}} \mathbf{Z_{Th}^{\pm}} \right) \Delta \mathbf{I_{dq}^m} + \mathbf{m_{dq0}^m} \Delta V_{dc}, \tag{14}$$

which can be rewritten as

$$\Delta \mathbf{I_{dq}^m} = \left[-\mathbf{Z_c^{\pm}} - \mathbf{Z_{Th}^{\pm}} - \mathbf{Z_{pi}^{\pm}} + \mathbf{H_f^{\pm}} \mathbf{Z_{Th}^{\pm}} \right]^{-1} \mathbf{m_{dq0}^m} \Delta V_{dc}. \tag{15}$$

By replacing (15) in (13), the DC admittance function is

$$\Delta I_{dc} = Y_{dc} \Delta V_{dc} \quad \mathbf{Z_{cf}^{\pm}} = \mathbf{Z_{pi}^{\pm}} - \mathbf{H_f^{\pm}} \mathbf{Z_{Th}^{\pm}}$$
$$Y_{dc} = \left((\mathbf{m_{dq0}^m}^T)^* + \frac{(\mathbf{I_{dq0}^m})^H}{V_{dc0}} \mathbf{Z_{cf}^{\pm}} \right) (\mathbf{Z_t^{\pm}} + \mathbf{Z_{cf}^{\pm}})^{-1} \mathbf{m_{dq0}^m}. \tag{16}$$

The DC admittance in (16) can finally be expressed as

$$Y_{dc} = \frac{3M^2}{4} \left(\frac{1}{\mathbf{Z_t^+} + \mathbf{Z_{cf}^+}} + \frac{1}{\left(\mathbf{Z_t^+} + \mathbf{Z_{cf}^+} \right)^*} \right)$$
$$+ \frac{1}{2V_{dc0}} \left[\frac{(I_{d0} - jI_{q0})(m_{d0} + jm_{q0}) \mathbf{Z_{cf}^+}}{\mathbf{Z_t^+} + \mathbf{Z_{cf}^+}} + \frac{(I_{d0} + jI_{q0})(m_{d0} - jm_{q0})(\mathbf{Z_{cf}^+})^*}{(\mathbf{Z_t^+})^* + (\mathbf{Z_{cf}^+})^*} \right], \tag{17}$$

where

$$\mathbf{Z_{cf}^+} = D(s) \left[F_{cc}(s) - jL_c \omega_1 - H_f(s) Z_{Th}(s + j\omega_1) \right]$$
$$(\mathbf{Z_{cf}^+})^* = D(s) \left[F_{cc}(s) + jL_c \omega_1 - H_f(s) Z_{Th}(s - j\omega_1) \right], \tag{18}$$

and the DC impedance is calculated with the inverse of the DC admittance, $\mathbf{Z_{DC}} = 1/\mathbf{Y_{DC}}$. The DC impedance in the previous simplified models, (8) and (17), is numerically validated by PSCAD/EMTDC simulation.

Figure 3 shows these DC impedances (see data in Table 2). The case without current control, $\mathbf{Z_{WC}}$, calculated with (8), is plotted with a solid line whereas the frequency response obtained by PSCAD/EMTDC simulation is plotted with crosses. The DC impedance case with current control, $\mathbf{Z_{CC}}$, calculated with (17), is represented in the same way. The accurate results of the DC-side equivalent admittance obtained with the proposed model are worth noting.

In the case without current control, the coupling between the DC and AC sides is revealed by the two peak values of $\mathbf{Z_{WC}}$. The DC-impedance $\mathbf{Z_{WC}}$ is affected by the mirror frequency effect. This is reflected in the expression of $\mathbf{Y_{DC}}$ (8) (see (1) in [12]), which depends on the impedances $Z_t(s + j\omega_1)$ and $Z_t(s - j\omega_1)$. As can be seen in the DC-impedance $\mathbf{Z_{CC}}$ in Figure 3, the control damps this coupling effect between the DC and AC sides [13].
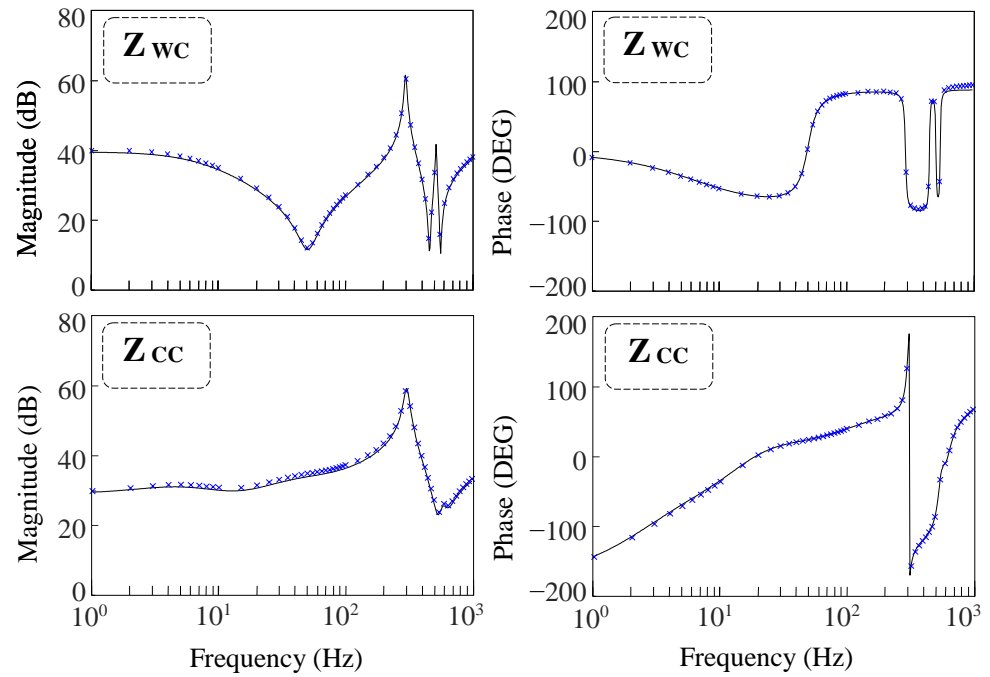
Figure 3. DC-impedance in the case without control, $\mathbf{Z_{WC}}$, and with current control, $\mathbf{Z_{CC}}$. (Lines: inverse of (8) and (17). Cross: PSCAD/EMTDC simulations.)

Table 2. AC Grid and VSC Parameters.

V_{ga}	$12.25/\sqrt{2}$ kV	P_{vsc}	30 MW	R_f, L_f	2.3 Ω, 0.18 mH
V_{dc0}	30 kV	R_g, L_g	0.52 Ω, 7.8 mH	R_c, L_c	0, 4 mH
C_f	35 μF	f_{sw}, T_d	10 kHz, 0.3 ms	I_{d0}, I_{q0}	−1996.3 A, 0 A
α_f	106.18 s^{-1}	m_{d0}	0.5168 pu	m_{q0}	0.0836 pu
$k_{p,cc}$	2 pu	$k_{p,dc}$	0.8662 pu	$k_{p,pll}$	0.2757 pu
$k_{i,cc}$	0.096 pu	$k_{i,dc}$	0.0334 pu	$k_{i,pll}$	0.2203 pu
$k_{p,ac}$	0.9 pu	$k_{p,P}$	0.13 pu	$k_{p,Q}$	0.13 pu
$k_{i,ac}$	0.008 pu	$k_{i,P}$	0.0083 pu	$k_{i,Q}$	0.0083 pu

3. Detailed Model of DC Admittance of VSCs

The PLL and the outer loop relations are included in the detailed model, where the current control loop is modified to account for the PLL effect. Now, the current control loop relations must consider the relationship between the variables in the converter *dq*-domain, which has the superscript "c", and the variables in the grid *dq*-domain, where no superscript is used. The current control loop [20] is expressed as

$$\Delta \mathbf{V_{dq,\,r}^{cm}} = -\mathbf{F_{cc}^{\pm}}\left(\Delta \mathbf{I_{dq,\,r}^{cm}} - \Delta \mathbf{I_{dq}^{cm}}\right) - \mathbf{Z_{\omega}^{\pm}}\Delta \mathbf{I_{dq}^{cm}} + \mathbf{H_f^{\pm}}\Delta \mathbf{E_{dq}^{cm}}. \tag{19}$$

The *dq*-complex space vector of the VSC reference voltage is written as $\mathbf{\Delta V^{cm}_{dq,\,r}} = V_{dc0}\mathbf{\Delta m^{cm}_{dq}}$. The PLL relations [9,20] are expressed as

$$\Delta \mathbf{I_{dq}^{cm}} = \Delta \mathbf{I_{dq}^{m}} + \mathbf{G_{PLLi}^{\pm}}\Delta \mathbf{E_{dq}^{m}}$$
$$\mathbf{G_{PLLi}^{+}} = -\mathbf{G_{PLLi}^{-}} = -G_{PLL}(s)(I_{d0}+jI_{q0})/2, \tag{20}$$

$$\Delta \mathbf{E_{dq}^{cm}} = \mathbf{G_{PLLv}^{\pm}}\Delta \mathbf{E_{dq}^{m}}$$
$$\mathbf{G_{PLLv}^{+}} = 1 - G_{PLL}(s)(E_{d0}+jE_{q0})/2$$
$$\mathbf{G_{PLLv}^{-}} = 1 - \mathbf{G_{PLLv}^{+}} = G_{PLL}(s)(E_{d0}+jE_{q0})/2, \tag{21}$$

$$
\begin{aligned}
\Delta \mathbf{m_{dq}^{cm}} &= \Delta \mathbf{m_{dq}^{m}} + \mathbf{G_{PLLm}^{\pm}} \Delta \mathbf{E_{dq}^{m}} \\
\mathbf{G_{PLLm}^{+}} &= -\mathbf{G_{PLLm}^{-}} = -G_{PLL}(s)(m_{d0} + jm_{q0})/2,
\end{aligned}
\tag{22}
$$

where $G_{pll}(s) = F_{pll}(s)/(s + V_{d0}F_{pll}(s))$, $F_{pll}(s) = k_{p,\,pll} + k_{i,\,pll}/s$, and $k_{p,\,pll}$ and $k_{i,\,pll}$ are the proportional and integral gains of the PLL control.

The reference currents generated by the outer control loops are related to the DC voltage and the input AC voltage and current of the VSC with *dq*-complex space vectors as the following general expression:

$$
\Delta \mathbf{I_{dq,\;r}^{cm}} = -\mathbf{F_o^m} \Delta V_{dc} - \mathbf{G_o^{\pm}} \Delta \mathbf{I_{dq}^{cm}} - \mathbf{Y_o^{\pm}} \Delta \mathbf{E_{dq}^{cm}},
\tag{23}
$$

where the complex transfer matrices $\mathbf{F^m_o}$, $\mathbf{G^{\pm}_o}$, and $\mathbf{Y^{\pm}_o}$ are the complex transfer matrices depending on the VSC operation mode (see Appendix A).

The outer control loop (23) can be introduced into the inner current control loop (19) as

$$
V_{dc0}\Delta \mathbf{m_{dq}^{cm}} = \Delta \mathbf{V_{dq,\;r}^{cm}} = \mathbf{F_{cc}^{\pm}F_o^m}\Delta V_{dc} + \left(\mathbf{Z_{pi}^{\pm}} + \mathbf{F_{cc}^{\pm}G_o^{\pm}}\right)\Delta \mathbf{I_{dq}^{cm}} + \left(\mathbf{H_f^{\pm}} + \mathbf{F_{cc}^{\pm}Y_o^{\pm}}\right)\Delta \mathbf{E_{dq}^{cm}},
\tag{24}
$$

where (24) is expressed in the converter *dq*-complex domain. By considering the PLL relations (20), (21), and (22) in the grid *dq*-domain (where no superscript is used), (24) becomes

$$
\begin{aligned}
\Delta \mathbf{m_{dq}^{m}} &= \tfrac{1}{V_{dc0}}\left\{ \mathbf{F_{cc}^{\pm}F_o^m}\Delta V_{dc} + (\mathbf{Z_{pi}^{\pm}} + \mathbf{F_{cc}^{\pm}G_o^{\pm}})\Delta \mathbf{I_{dq}^{m}} + \mathbf{H_o^{\pm}}\Delta \mathbf{E_{dq}^{m}} \right\} \\
\mathbf{H_o^{\pm}} &= (\mathbf{Z_{pi}^{\pm}} + \mathbf{F_{cc}^{\pm}G_o^{\pm}})\mathbf{G_{plli}^{\pm}} + (\mathbf{H_f^{\pm}} + \mathbf{F_{cc}^{\pm}Y_o^{\pm}})\mathbf{G_{pllv}^{\pm}} - V_{dc0}\mathbf{G_{pllm}^{\pm}},
\end{aligned}
\tag{25}
$$

and introducing (1) into (25) results in

$$
\Delta \mathbf{m_{dq}^{m}} = \frac{1}{V_{dc0}}\left\{ \mathbf{F_{cc}^{\pm}F_o^m}\Delta V_{dc} + (\mathbf{Z_{pi}^{\pm}} + \mathbf{F_{cc}^{\pm}G_o^{\pm}} - \mathbf{H_o^{\pm}Z_{Th}^{\pm}})\Delta \mathbf{I_{dq}^{m}} \right\}.
\tag{26}
$$

The DC voltage in (4) can be related to the AC current from (26) and the AC grid relations (1) and (2) as follows:

$$
\Delta \mathbf{V_{dq}^{m}} = -(\mathbf{Z_c^{\pm}} + \mathbf{Z_{Th}^{\pm}})\Delta \mathbf{I_{dq}^{m}} = (\mathbf{m_{dq0}^{m}} + \mathbf{F_{cc}^{\pm}F_o^m})\Delta V_{dc} + (\mathbf{Z_{pi}^{\pm}} + \mathbf{F_{cc}^{\pm}G_o^{\pm}} - \mathbf{H_o^{\pm}Z_{Th}^{\pm}})\Delta \mathbf{I_{dq}^{m}}.
\tag{27}
$$

By using (1), (25) is rewritten as

$$
\begin{aligned}
\mathbf{G_V}\Delta V_{dc} &= -\mathbf{Z_V}\Delta \mathbf{I_{dq}^{m}} & \mathbf{G_V} &= \mathbf{m_{dq0}^{m}} + \mathbf{F_{cc}^{\pm}F_o^m} \\
\mathbf{Z_V} &= \mathbf{Z_t^{\pm}} + \mathbf{Z_a^{\pm}} & \mathbf{Z_a^{\pm}} &= \mathbf{Z_{pi}^{\pm}} + \mathbf{F_{cc}^{\pm}G_o^{\pm}} - \mathbf{H_o^{\pm}Z_{Th}^{\pm}}.
\end{aligned}
\tag{28}
$$

The DC current in (5) can be related to the AC current using (25) and the AC grid relations (1) and (2) as follows:

$$
\Delta I_{dc} = -(\mathbf{m_{dq0}^{m}}{}^T)^* \Delta \mathbf{I_{dq}^{m}} - \frac{(\mathbf{I_{dq0}^{m}})^H}{V_{dc0}}\left\{ \mathbf{F_{cc}^{\pm}F_o^m}\Delta V_{dc} + \mathbf{Z_a^{\pm}}\Delta \mathbf{I_{dq}^{m}} \right\},
\tag{29}
$$

which can be rewritten as

$$
\Delta I_{dc} = -\mathbf{Y_I}\Delta V_{dc} - \mathbf{G_I}\Delta \mathbf{I_{dq}^{m}} \quad \mathbf{Y_I} = \frac{(\mathbf{I_{dq0}^{m}})^H}{V_{dc0}}\mathbf{F_{cc}^{\pm}F_o^m} \quad \mathbf{G_I} = (\mathbf{m_{dq0}^{m}}{}^T)^* + \frac{(\mathbf{I_{dq0}^{m}})^H}{V_{dc0}}\mathbf{Z_a^{\pm}}.
\tag{30}
$$

The DC-admittance $Y_{dc} = \Delta I_{dc}/\Delta V_{dc}$ is obtained from the DC voltage and current relations (28) and (30), respectively, resulting in

$$
Y_{dc} = \frac{\Delta I_{dc}}{\Delta V_{dc}} = -\mathbf{Y_I} + \mathbf{G_I Z_V^{-1} G_V} = -\frac{(\mathbf{I_{dq0}^{m}})^H}{V_{dc0}}\mathbf{F_{cc}^{\pm}F_0^m} + \left((\mathbf{m_{dq0}^{m}})^H + \frac{(\mathbf{I_{dq0}^{m}})^H}{V_{dc0}}\mathbf{Z_a^{\pm}}\right)(\mathbf{Z_t^{\pm}} + \mathbf{Z_a^{\pm}})^{-1}(\mathbf{m_{dq0}^{m}} + \mathbf{F_{cc}^{\pm}F_0^m}).
\tag{31}
$$

PSCAD/EMTDC simulations were performed to study the DC impedance calculation accuracy of different control modes. The parameters of each case are listed in Table 2. Figure 4 shows the DC impedance in the case of the outer control mode $P - Q$, Z_{PQ} and $P - E_{ac}$, Z_{PE}. Figure 5 shows the DC impedance in the case of the outer control mode $V_{dc} - Q$, Z_{UQ} and $V_{dc} - E_{ac}$, Z_{UE}. The simulation data are shown with x crosses in Figures 4 and 5. The continuous curves are calculated from the inverse of (31) and they fit well with the simulation results.
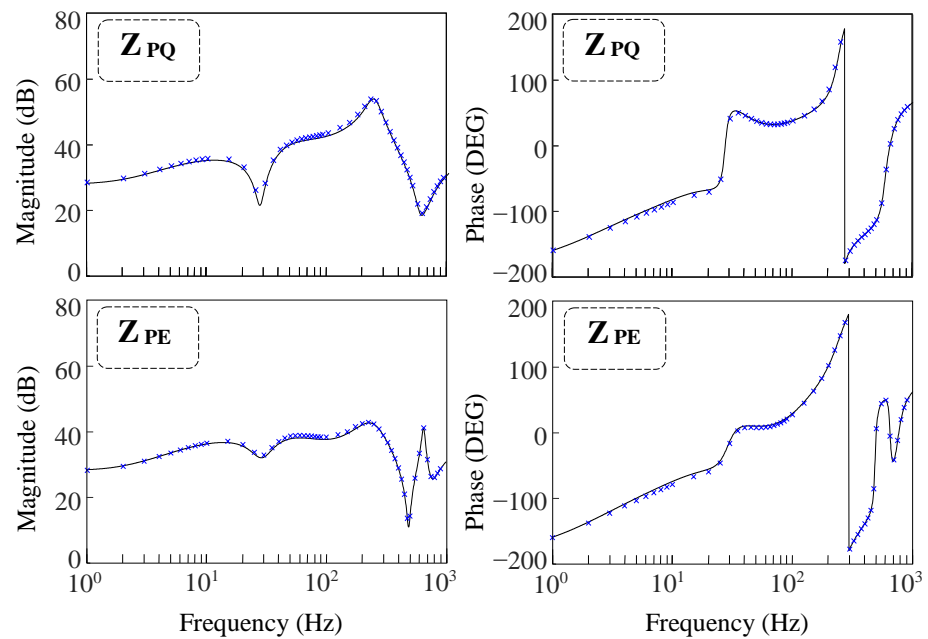
Figure 4. DC-impedance of P-Q and P-E control modes. (Lines: inverse of (31). Cross: PSCAD/ EMTDC simulations.)
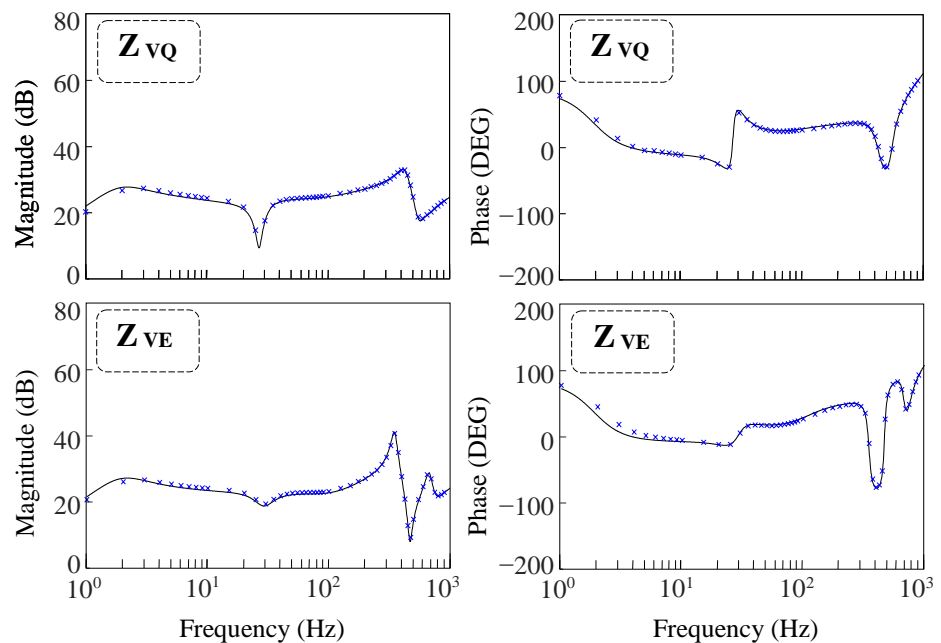

Figure 5. DC-impedance of V_{dc}-Q and V_{dc}-E control modes. (Lines: inverse of (31). Cross: PSCAD/EMTDC simulations.)

4. Impedance-Based Stability Criteria

Once the DC-side equivalent admittance of VSCs is obtained, the general HVDC interconnected system in Figure 6a can be considered for stability studies. The incremental symbol Δ of the small-signal variables is omitted for the sake of simplicity. The external components connected to the DC grid buses are represented by their equivalent circuits as follows:

- Grid-connected VSCs are characterized by the current balance at their Norton equivalent circuit buses:

$$I_i = I_{dc,i} - Y_{dc,i}(s)V_i \ (i = 1, \dots a), \tag{32}$$

where the expression of $Y_{dc,i}(s)$ is the DC admittance in (31).

- DC loads are characterized by their admittance transfer function $Y_i(s)$ ($i = 1, \dots b$).
- Terminals without any connected external component are represented as open-circuit buses characterized by zero values of the current source and admittance of the Norton equivalent circuit, $I_i = Y_i(s) = 0$ ($i = 1, \dots c$).

Several impedance-based stability criteria are proposed in the literature [1–10]. Some of the differences between these criteria are discussed in [2]. This discussion is extended in the sections below considering the general DC system in Figure 6a where $Y_{dc,i}(s)$ (31) is used to assess DC interconnected system stability. The discussion is also supported by Section 5.
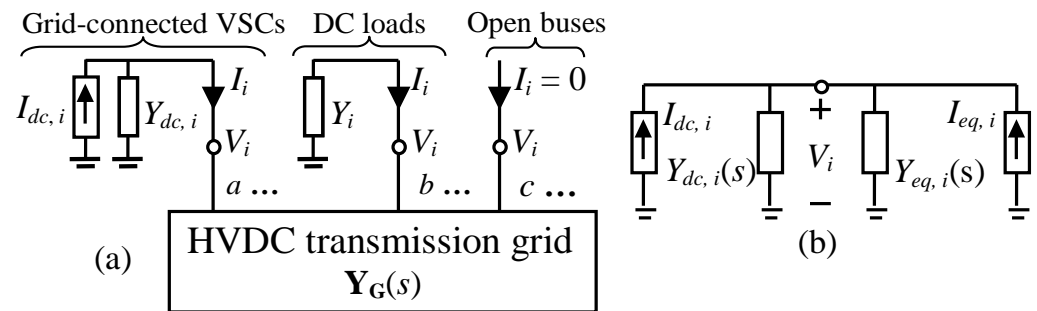

Figure 6. Stability assessment in HVDC transmission grids: (**a**) HVDC transmission grid. (**b**) SISO equivalent system partitioned at VSC terminals.

4.1. Norton Admittance Matrix-Based Stability Assessment

The relations between voltages and currents at the HVDC transmission grid terminals in Figure 6a are expressed as

$$\left. \begin{array}{c} \mathbf{i} = \mathbf{Y_G}(s)\mathbf{v} \\ \mathbf{i} = \mathbf{i_E} - \mathbf{Y_E}(s)\mathbf{v} \end{array} \right\} \ \Rightarrow \ \mathbf{v} = (\mathbf{Y_G}(s) + \mathbf{Y_E}(s))^{-1}\mathbf{i_E}, \tag{33}$$

where $\mathbf{Y_G}(s)$ is the admittance matrix of the HVDC transmission grid; $\mathbf{i_E}$ and $\mathbf{Y_E}(s)$ are the current source and the diagonal admittance matrix of the external components, respectively; and $\mathbf{v}$ and $\mathbf{i}$ are the voltage and the injected current at the grid terminals, respectively.

Stability can be analyzed in the frequency domain by rewriting (33) as

$$\mathbf{v} = (\mathbf{I} + \mathbf{Z_G}(s)\mathbf{Y_E}(s))^{-1}\mathbf{Z_G}(s)\mathbf{i_E}, \tag{34}$$

where $\mathbf{I}$ is the identity matrix, and $\mathbf{Z_G}(s) = \mathbf{Y_G}^{-1}(s)$ is the grid impedance matrix. The stability of the closed-loop system in (34) can be assessed by the GNC if and only if $\mathbf{L}(s)$ does not have a right-half-plane (RHP) pole. This criterion (called SC_1 in this paper) extends the traditional Nyquist criterion to the Nyquist curves of the eigenvalues of the loop transfer function $\mathbf{L}(s) = \mathbf{Z_G}(s)\mathbf{Y_E}(s)$ [2,6,10,12,13]. Note that the RHP pole condition fails when system instability comes from the AC side of any VSC because the corresponding

VSC subsystem in the diagonal of $\mathbf{Y_E}(s)$ is unstable. This instability was not detected in this case and, obviously, was also not detected when AC grid dynamics were disregarded in the DC-side equivalent admittance modeling of the VSCs.

4.2. SISO-Based Stability Assessment

The SISO system in Figure 6b can be derived at the VSC terminals, where $I_{eq,\,i}$ and $Y_{eq,\,i}(s)$ represent the current source and the admittance of the DC grid equivalent circuit observed from any VSC. The relation between the voltage V_i and the current sources is expressed as

$$V_i = Z_t(s)(I_{dc,\,i} + I_{eq,\,i}) \;\; ; \;\; Z_t(s) = \frac{1}{Y_{eq,\,i}(s) + Y_{dc,\,i}(s)}. \tag{35}$$

Two approaches are used to assess the stability of the SISO closed-loop system in (35):

- **Impedance-ratio stability criterion**

Stability can be analyzed in the frequency domain by rewriting (35) as

$$V_i = \frac{Z_{eq,\,i}(s)}{1 + Z_{eq,\,i}(s)Y_{dc,\,i}(s)}(I_{dc,\,i} + I_{eq,\,i}) = Z_{T,\,i}(s)I_{T,\,i}. \tag{36}$$

If and only if the impedance ratio $Z_{eq,\,i}(s) \cdot Y_{dc,\,i}(s)$ does not have a right-half-plane (RHP) pole, the stability of the closed-loop system in (36) can be assessed by the Nyquist stability criterion (denoted as SC in this paper), which evaluates the Nyquist curve of the impedance ratio [4–6,9,11,15]. This criterion can only be applied if instability comes from the interaction between the VSC and the DC grid equivalent circuit because the RHP pole condition fails when system instability comes from the AC side of the VSC or the DC grid equivalent circuit observed from the VSC.

- **Positive-net-damping stability criterion**

The positive-net-damping stability criterion (denoted as SC_3 in this paper) evaluates system transfer impedance damping in (36) at resonance frequencies, i.e., the value of $Re\{Z_{T,\,i}(j\omega)\}$ at the frequencies of the peak values of $Z_{T,\,i}(j\omega)$ [4–9]. This criterion assesses the closed-loop transfer function of the system, which avoids inaccuracies derived from local instabilities in the stability conclusion.

5. Application

The stability in the VSC-HVDC system of Figure 7a was studied. Two converter stations, VSC_1 and VSC_2, were connected through a 1000 MW 440 kV HVDC transmission grid. VSC_1 operated in mode $V_{dc} - Q$, controlling the DC voltage of the HVDC transmission grid, whereas VSC_2 operated in mode $P - Q$, controlling the transmitted active power. Both converters worked at unity power factor, typical of normal operating conditions [8,12–15]. According to Figure 7b, VSC_1 is characterized by the DC-side equivalent admittance in (31), while VSC_2 is considered as constant power consumption P_{20} characterized by the fictive resistance $R_{20} = -(V_{dc2,\,0})^2/P_{20}$ [4,9]. This converter could also be characterized with the DC-side equivalent admittance in (31), but a simpler model was used in the stability study to focus the attention on VSC_1. VSC-HVDC system data are in Table 3. Three cases were studied in the application:

- Case #1 (stable reference case): this corresponds to the data in Table 3, with the power consumed by VSC_2 being half the nominal power (i.e., P_{20} = 500 MW).
- Cases #2 and #3: the influence of the short-circuit ratio *SCR* and the VSC_2-consumed power P_{20}, respectively, on system stability were analyzed.
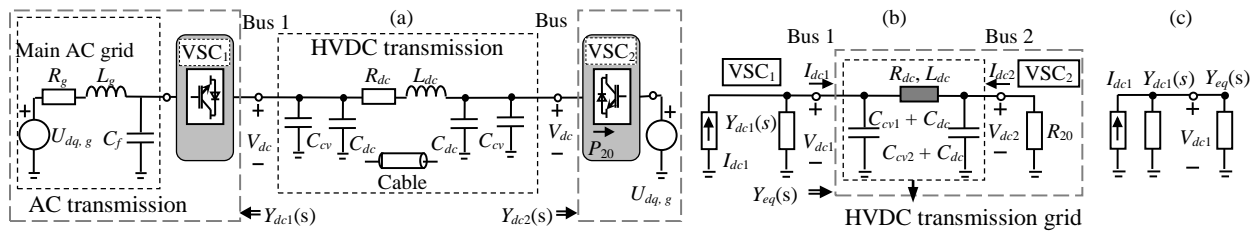
Figure 7. HVDC application: (**a**) HVDC transmission system. (**b**) HVDC transmission grid with VSC equivalent admittances. (**c**) Equivalent HVDC circuit.

Table 3. VSC-HVDC System Data ($U_{B,\,AC}$ = 220 kV, $U_{B,\,DC}$ = 440 kV, S_B = 1000 MVA).

AC main grid	U_0 (f_1), X_g/R_g $SCR = S_{cc}/(P_{vsc1,\,N})$	220 kV (50 Hz), 20 pu 15 pu
VSC AC filter	C_f	6 MF
DC cable	R_{dc}, L_{dc} C_{dc}, Length	10.8 mΩ/km, 0.149 mH/km 0.145 MF/km, 25 km
VSC DC filters	C_{cvi} (i = 1 to 2)	30 MF
VSC$_1$	$P_{vsc1,\,N}$, $V_{dc1,\,0}$	1000 MW, 440 kV
VSC$_1$ control	f_s, T_d R_c, L_c $k_{p,cc}$, $k_{i,cc}$ $k_{p,pll}$, $k_{i,pll}$ $k_{p,dc}$, $k_{i,dc}$ $k_{p,p}$, $k_{i,p}$	2 kHz, 0.3 ms 0.025 pu, 0.25 pu 1.21 pu, 0.121 pu 0.48 pu, 0.031pu 0.15 pu, 0.058 pu 0.15 pu, 0.058 pu

The system stability was verified by PSCAD/EMTDC time-domain simulations, and the predictions obtained by the stability criteria SC$_1$, SC$_2$, and SC$_3$ in Section 4 were investigated. The results are shown in Figures 8 and 9.
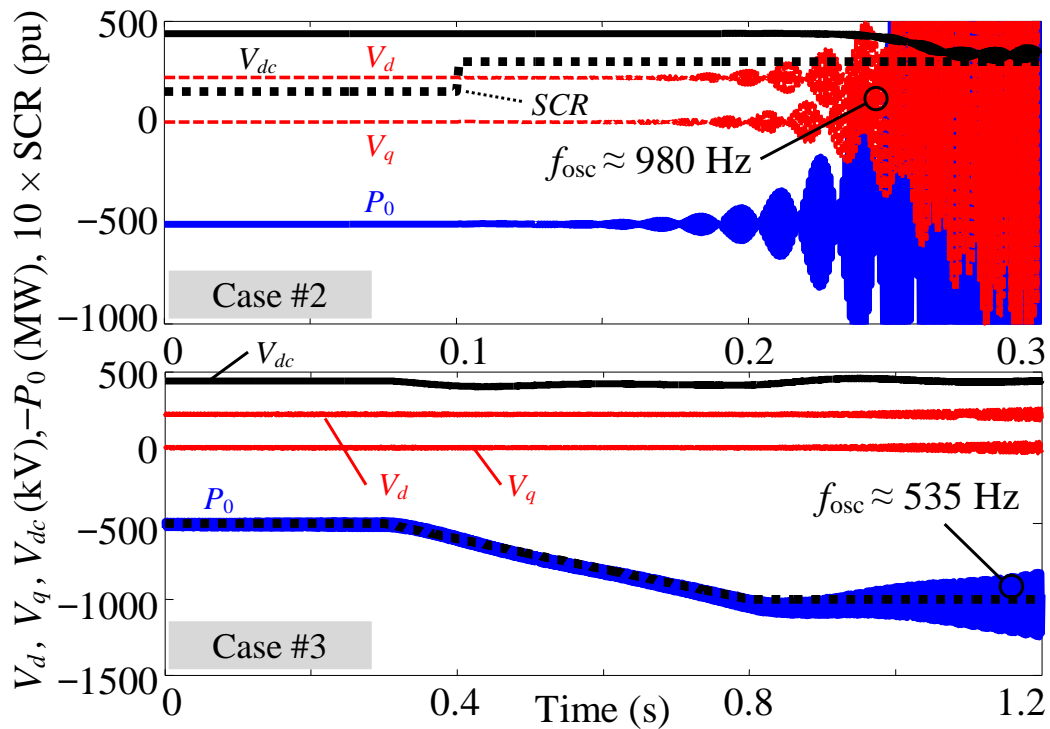

Figure 8. Stability study: Case #2 (top) and Case #3 (bottom).
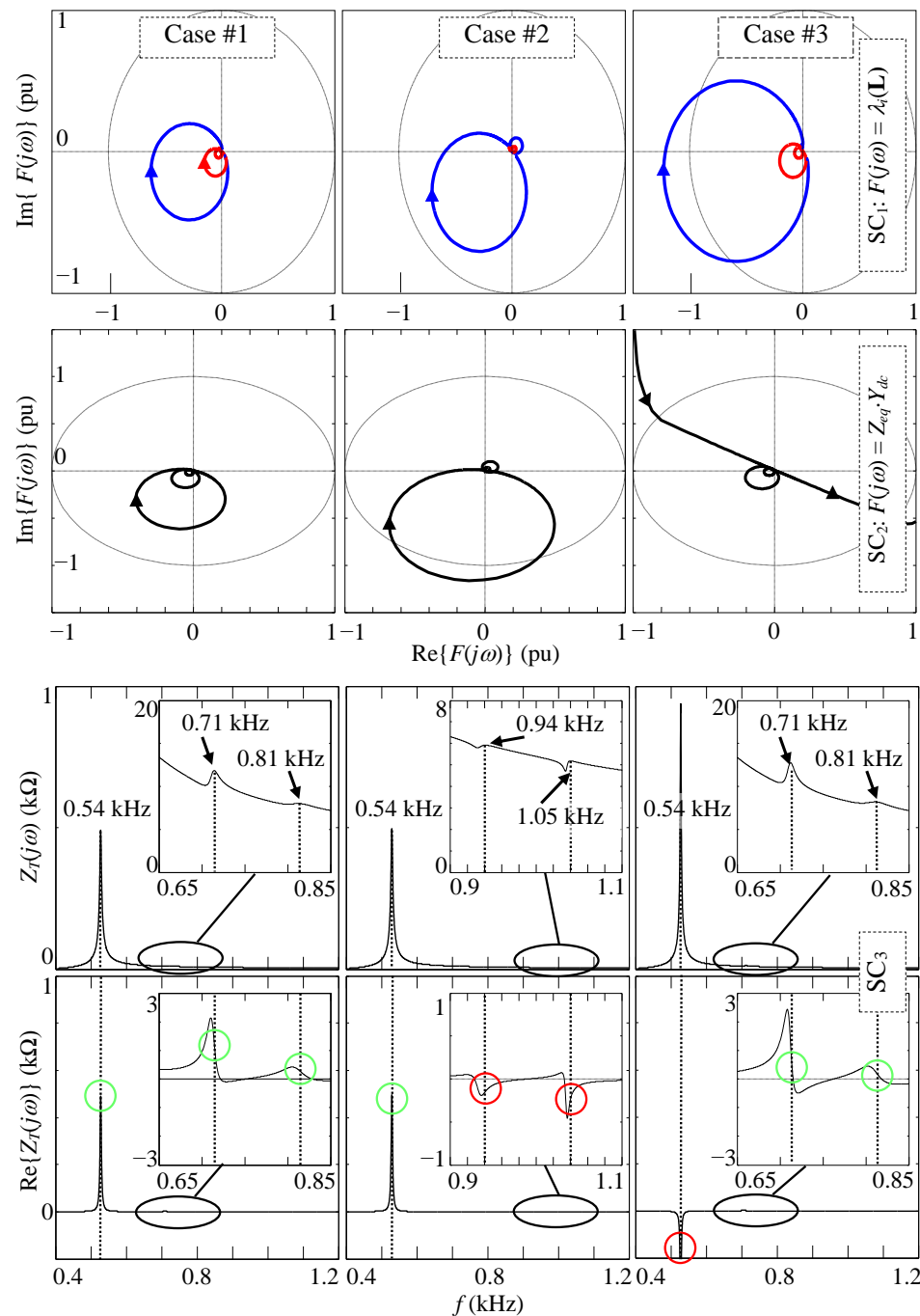
Figure 9. Impedance-based stability study.

Case #1: The PSCAD/EMTDC simulations before *SCR* and P_{20} changes in Figure 8 show the system stability. The results obtained from the stability criteria are as follows (see Figure 9, left):

- SC_1: the GNC verifies system stability because the curves of the eigenvalues of $\mathbf{L}(s)$ do not encircle the -1 point.
- SC_2: the Nyquist criterion verifies system stability because the Nyquist curve of $Z_{eq,i}Y_{dc,i}$ does not encircle the -1 point.
- SC_3: The positive-net-damping stability criterion verifies system instability because the damping $\text{Re}\{Z_T(j\omega)\}$ at resonance frequencies $f_r \approx 537.5$, 712.3 and 810.3 Hz is positive. The first resonance is due to the HVDC grid capacitors and inductors whereas the second and third resonances are at the DC mirror resonance frequencies of the

AC-side resonance between the AC grid inductance L_g and the VSC$_1$ filter capacitor C_f at f_r = 760 Hz. It is observed that the VSC control damps (but does not eliminate) the AC-side resonance at the DC side. This means that AC-side dynamics are only damped at the DC side by the VSC control and should therefore be considered in the DC-side equivalent admittance modeling of the VSCs [12,13].

Case #2: The short-circuit ratio *SCR* increases from 15 pu to 30 pu at 0.1 s. The PSCAD/EMTDC simulation in Figure 8 shows that the system becomes unstable after the *SCR* value steps up. It was numerically verified that this is because the AC system resonance frequency is shifted to a negative damping frequency range and the AC-side voltage oscillations at $f \approx 980$ Hz are amplified. The results obtained by the stability criteria are as follows (see Figure 9, middle):

- SC$_1$: the GNC leads to an inaccurate stability assessment (i.e., the curves of the eigenvalues of **L**(s) do not encircle the -1 point) because the instability comes from the AC system resonance, causing the DC-admittance $Y_{dc,1}(s)$ in the diagonal of **Y$_E$** (s) to be unstable.
- SC$_2$: the Nyquist criterion also leads to an inaccurate stability assessment because $Y_{dc,1}(s)$ is unstable [13].
- SC$_3$: The positive-net-damping stability criterion verifies system stability (i.e., Re{$Z_T(j\omega)$} is negative at mirror resonance frequencies $f_r \approx 935.5$ and 1045 Hz). Closed-loop transfer function assessment by the positive-net-damping stability criterion avoids the SC$_1$ and SC$_2$ stability inaccuracy derived from the instability of $Y_{dc,1}(s)$. If AC-side dynamics are disregarded in the DC-side equivalent admittance model, AC-side resonances are overlooked, which leads to inaccurate stability assessments [12,13].

Case #3: The VSC$_2$-consumed active power increases from P_{20} = 500 MW to the nominal value P_{20} = 1000 MW at 0.3 s. The PSCAD/EMTDC simulation in Figure 8 shows that the system becomes unstable after the P_{20} value ramps up. It was numerically verified that this is because the damping becomes negative at the DC resonance frequency, and the DC-side voltage oscillations at $f \approx 535$ Hz are amplified. The results obtained by the stability criteria are as follows (see Figure 9, right):

- SC$_1$: the GNC verifies system instability because the curve of one eigenvalue intersects the unit circle at approximately 527 Hz, enclosing the -1 point in a clockwise direction.
- SC$_2$: the Nyquist criterion leads to an inaccurate stability assessment because of instability in $Y_{eq,1}(s)$.
- SC$_3$: The positive-net-damping stability criterion verifies system instability (i.e., Re{$Z_T(j\omega)$} is negative at $f_r \approx 537$ Hz). The closed-loop transfer function assessment in the positive-net-damping stability criterion avoids the SC$_2$ stability inaccuracy derived from the instability of $Y_{eq,1}(s)$.

6. Comparison of DC Admittance Models

The influence of the different simplifications that are usually carried out in DC admittance models is shown in Table 4. The results obtained with the full model in Section 3 for the three cases in Section 4 were compared with those obtained considering five different simplifications. It can be observed that the simplification of the *d*-outer control loop and the PLL do not affect the results of the full model, while this is not true for the simplifications related to the inner control loop (i.e., the VSC delay and the bandwidth of the grid voltage feedforward simplifications). Nevertheless, it must be noted that the above conclusions correspond to the harmonic instabilities of the studied cases, and they cannot be extrapolated to other types of instabilities. In general, harmonic instabilities are mainly affected by the inner control loop parameters, while synchronous and subsynchronous instabilities are affected by the outer control loops and the PLL.

Table 4. Comparison of simplifications.

	Cases		
Model Feature	**Case #1**	**Case #2**	**Case #3**
Full model	Stable	Instable	Instable
No phase-locked loop control	Stable	Instable	Instable
No VSC delay	Stable	Stable	Stable
No grid voltage feedforward ($\alpha_f = 0$)	Stable	Stable	Instable
No grid voltage feedforward filter ($\alpha_f = \infty$)	Stable	Instable	Instable
No d-outer control loop	Stable	Instable	Instable

7. Conclusions

This paper presents a complete and detailed DC admittance model for VSC rectifier and inverter stations of VSC-HVDC systems with active power, DC voltage, grid alternating voltage, and reactive power controls. The model also considers the VSC delay, grid voltage feedforward filter, PLL, and several outer control loops. It is derived from dq-complex space vectors commonly used in circuit theory. A comparison between the different models in the literature and a study of the impact on the instability of the different model simplifications were carried out to illustrate the contribution of the paper. The proposed model was applied to discuss VSC-HVDC system stability and the inaccuracies of impedance-based stability criteria due to system partitions. It is concluded that the stability assessment of VSC-HVDC systems from VSC and DC grid equivalent circuits could lead to inaccurate conclusions by the Nyquist criterion (e.g., when instability comes from AC-side dynamics) whereas the positive-net-damping criterion overcomes this issue because it is a global stability criterion which evaluates system transfer impedance damping at resonance frequencies.

Author Contributions: Conceptualization and methodology, J.P. and L.S.; software development and validation, L.M. and J.P.; writing—original draft preparation, J.P. and L.S.; visualization, L.M. All authors have read and agreed to the published version of the manuscript.

Appendix A. Outer Loop Controls

The VSC control is characterized by the current controller (CC) and the outer control loops, which make it possible to characterize the main VSC operation modes (i.e., mode $P - Q$, mode $V_{dc} - Q$, mode $V_{dc} - E_{ac}$, and mode $P - E_{ac}$) [8].

$\underline{V_{dc} - Q}$ **control:** the direct voltage control (DVC) and reactive power control (QPC) of Figure 1 are expressed with dq-complex space vectors [20] using the notation of (23) as

$$\mathbf{F_{o,\,UQ}^m} = \frac{1}{\sqrt{2}}\begin{bmatrix} F_{dc}(s) \\ F_{dc}(s) \end{bmatrix} \;;\; \mathbf{G_{o,\,UQ}^{\pm}} = \frac{F_q(s)E_{d0}}{2}\begin{bmatrix} 1 & -1 \\ -1 & 1 \end{bmatrix} \;;\; \mathbf{Y_{o,\,UQ}^{\pm}} = \frac{F_q(s)}{\sqrt{2}}\begin{bmatrix} -\mathbf{I_{dq0}^*} & \mathbf{I_{dq0}} \\ \mathbf{I_{dq0}^*} & -\mathbf{I_{dq0}} \end{bmatrix}, \tag{A1}$$

where $F_{dc}(s) = k_{p,\,dc} + k_{i,\,dc}/s$, with $k_{p,\,dc}$ and $k_{i,\,dc}$ being the proportional and integral gains of the DVC, and $F_p(s) = k_{p,\,q} + k_{i,\,q}/s$, with $k_{p,\,q}$, and $k_{i,\,q}$ being the proportional and integral gains of the QPC.

$\underline{P - Q}$ **control:** the alternating power control (APC) and reactive power control of Figure 1 are expressed with dq-complex space vectors [20] using the notation of (23) as

$$\mathbf{G_{o,\,PQ}^{\pm}} = F_p(s)E_{d0}\begin{bmatrix} 1 & 0 \\ 0 & 1 \end{bmatrix} \;;\; \mathbf{Y_{o,\,PQ}^{\pm}} = \sqrt{2}F_p(s)\begin{bmatrix} 0 & \mathbf{I_{dq0}} \\ \mathbf{I_{dq0}^*} & 0 \end{bmatrix}, \tag{A2}$$

where $F_p(s) = k_{p,p} + k_{i,p}/s$, with $k_{p,p} = k_{p,q}$ and $k_{i,p} = k_{i,q}$ being the proportional and integral gains of the APC.

$V_{dc} - E_{ac}$ **control:** the direct voltage control (DVC) and alternating voltage control (AVC) control law of Figure 1 are expressed with *dq*-complex space vectors using the notation of (23) as

$$\mathbf{F}^{\mathbf{m}}_{\mathbf{o, UE}} = \frac{1}{\sqrt{2}} \begin{bmatrix} F_{dc}(s) \\ F_{dc}(s) \end{bmatrix} \ ; \ \mathbf{Y}^{\pm}_{\mathbf{o, UE}} = \frac{F_v(s)}{2} \begin{bmatrix} j & j \\ -j & -j \end{bmatrix}, \tag{A3}$$

where $F_v(s) = k_{p,v} + k_{i,v}/s$, with $k_{p,v}$ and $k_{i,v}$ being the proportional and integral gains of the AVC.

$\underline{P - E_{ac}}$ **control:** the alternating power control (APC) and alternating voltage control (AVC) control law of Figure 1 are expressed with *dq*-complex space vectors using the notation of (23) as

$$\mathbf{G}^{\pm}_{\mathbf{o, PE}} = \frac{F_p(s)E_{d0}}{2} \begin{bmatrix} 1 & 1 \\ 1 & 1 \end{bmatrix} \ ; \ \mathbf{Y}^{\pm}_{\mathbf{o, PE}} = \frac{F_p(s)}{\sqrt{2}} \begin{bmatrix} \mathbf{I}^{*}_{\mathbf{dq0}} & \mathbf{I}_{\mathbf{dq0}} \\ \mathbf{I}^{*}_{\mathbf{dq0}} & \mathbf{I}_{\mathbf{dq0}} \end{bmatrix} + \frac{F_v(s)}{2} \begin{bmatrix} j & j \\ -j & -j \end{bmatrix}. \tag{A4}$$

References

1. Sun, J.; Li, M.; Zhang, Z.; Xu, T.; He, J.; Wang, H.; Li, G. Renewable energy transmission by HVDC across the continent: System challenges and opportunities. *CSEE J. Power Energy Syst.* **2017**, *3*, 353–364. [CrossRef]
2. Zhang, C.; Molinas, M.; Rygg, A.; Cai, X. Impedance-Based Analysis of Interconnected Power Electronics Systems: Impedance Network Modeling and Comparative Studies of Stability Criteria. *IEEE J. Emerg. Sel. Top. Power Electron.* **2020**, *8*, 2520–2533. [CrossRef]
3. Liu, H.; Xie, X.; Liu, W. An Oscillatory Stability Criterion Based on the Unified *dq*-Frame Impedance Network Model for Power Systems with High-Penetration Renewables. *IEEE Trans. Power Syst.* **2018**, *33*, 3472–3485. [CrossRef]
4. Stamatiou, G.; Bongiorno, M. Stability Analysis of Two-Terminal VSC-HVDC Systems Using Net-Damping Criterion. *IEEE Trans. Power Deliv.* **2016**, *31*, 1748–1756. [CrossRef]
5. Sainz, L.; Cheah-Mane, M.; Monjo, L.; Liang, J.; Gomis-Bellmunt, O. Positive-net-damping Stability Criterion in Grid-connected VSC Systems. *IEEE J. Emerg. Sel. Top. Power Electron.* **2017**, *4*, 1499–1512. [CrossRef]
6. Harnefors, L. Modeling of Three-Phase Dynamic Systems Using Complex Transfer Functions and Transfer Matrices. *IEEE Trans. Ind. Electron.* **2007**, *54*, 2239–2248. [CrossRef]
7. Harnefors, L. Proof and Application of the Positive-net-damping Stability Criterion. *IEEE Trans. Power Syst.* **2011**, *26*, 481–482. [CrossRef]
8. Harnefors, L.; Bongiorno, M.; Lundberg, S. Input-admittance Calculation and Shaping for Controlled Voltage-source converters. *IEEE Trans. Ind. Electron.* **2007**, *54*, 3323–3334. [CrossRef]
9. Wen, B.; Boroyevich, D.; Burgos, R.; Mattavelli, P.; Shen, Z. Analysis of D-Q Small-Signal Impedance of Grid-Tied Inverters. *IEEE Trans. Power Electron.* **2016**, *31*, 675–687. [CrossRef]
10. Pinares, G.; Bongiorno, M. Analysis and Mitigation of Instabilities Originated from DC-side Resonances in VSC-HVDC Systems. *IEEE Trans. Ind. Appl.* **2016**, *52*, 2807–2815. [CrossRef]
11. Xu, L.; Fan, L.; Miao, Z. DC Impedance-model Based Resonance Analysis of a VSC-HVDC System. *IEEE Trans. Power Deliv.* **2015**, *30*, 1221–1230. [CrossRef]
12. Shah, S.; Parsa, L. Impedance Modeling of Three-phase Voltage Source Converters in dq, Sequence and Phasor Domains. *IEEE Trans. Energy Convers.* **2017**, *32*, 1139–1150. [CrossRef]
13. Amin, M.; Molinas, M. Small-signal Stability Assessment of Power Electronics Based Power Systems: A Discussion of Impedance- and Eigenvalue-based Methods. *IEEE Trans. Ind. Appl.* **2017**, *53*, 5014–5030. [CrossRef]
14. Amin, M.; Molinas, M.; Lyu, J.; Cai, X. Impact of Power Flow Direction on the Stability of VSC-HVDC Seen from the Impedance Nyquist Plot. *IEEE Trans. Power Electron.* **2017**, *32*, 8204–8217. [CrossRef]
15. Liu, J.; Tao, X.; Yu, M.; Xia, Y.; Wei, W. Impedance Modeling and Analysis of Three-Phase Voltage-Source Converters Viewing from DC Side. *IEEE J. Emerg. Sel. Top. Power Electron.* **2020**, *8*, 3906–3916. [CrossRef]
16. Rygg, A.; Molinas, M.; Zhang, C.; Cai, X. A Modified Sequence-domain Impedance Definition and its Equivalence to the dq-domain Impedance Definition for the Stability Analysis of AC Power Electronic Systems. *IEEE J. Emerg. Sel. Top. Power Electron.* **2016**, *4*, 1383–1396. [CrossRef]
17. Wang, X.; Harnefors, L.; Blaabjerg, F. Unified Impedance Model of Grid-connected Voltage-source Converters. *IEEE Trans. Power Electron.* **2018**, *33*, 1775–1785. [CrossRef]
18. Paap, G.C. Symmetrical Components in the Time Domain and their Application to Power Network Calculations. *IEEE Trans. Power Syst.* **2000**, *15*, 522–528. [CrossRef]

19. Harnefors, L.; Wang, X.; Chou, S.; Bongiorno, M.; Hinkkanen, M.; Routimo, M. Asymmetric Complex-Vector Models With Application to VSC–Grid Interaction. *IEEE J. Emerg. Sel. Top. Power Electron.* **2020**, *8*, 1911–1921. [CrossRef]
20. Pedra, J.; Sainz, L.; Monjo, L. Three-port small-signal admittance-based model of VSC for studies of multi-terminal HVDC hybrid AC/DC transmission grids. *IEEE Trans. Power Syst.* **2021**, *36*, 732–743. [CrossRef]